Bull Volcanol (2014) 76:829
DOI 10.1007/s00445-014-0829-3

RESEARCH ARTICLE

The influence of cross-sectional channel geometry on rheology and flux estimates for active lava flows

Einat Lev · Mike R. James

Received: 5 November 2013 / Accepted: 28 April 2014

Abstract Lava rheology and effusion rate are critical factors in determining the evolution of lava flows. However, direct and accurate field measurements are difficult to carry out, and estimates are usually based on measurements of the flow's surface velocity and assumptions of sub-surface geometry. Using numerical flow models, we show that the potential for error due to geometry uncertainty is minimized if a semi-elliptical cross-sectional channel shape is assumed. Flow is simulated for isothermal Newtonian, temperature-dependent Newtonian, and isothermal power-law rheology lavas. For isothermal Newtonian lava, we find that the error in channel shape alone can make apparent viscosity estimates ~3.5 times too large (e.g., for inappropriate use of the Jeffreys equation on a narrow semi-elliptical channel). For a temperature-dependent rheology, using an analytical approximation for Newtonian flow in a semi-elliptical geometry yields apparent viscosity and flux values that are more accurate than estimates which assume a rectangular geometry, for all channel shapes considered, including rectangular channels. Viscosity calculations for real channels on Mauna Loa and Mount Etna show that for a Newtonian rheology, a semi-elliptical analytical solution gives an approximation three times closer to the actual viscosity than a rectangle with the same depth while, if the lava is shear-thinning (power law exponent $m = 0.6$), a rectangular approximation is 15 % more accurate. Our results can be used to bracket possible viscosity and flux estimates when channel topography is poorly constrained.

Keywords Lava flows · Lava rheology · Channels · Numerical models

Editorial responsibility: M. R. Patrick

Electronic supplementary material The online version of this article (doi: 10.1007/s00445-014-0829-3) contains supplementary material, which is available to authorized users.

E. Lev (✉)
Lamont-Doherty Earth Observatory, Columbia University, New York, NY, USA
e-mail: einatlev@ldeo.columbia.edu

M. R. James
Lancaster Environment Centre, Lancaster University, Lancaster, UK

Introduction

Lava flows on Earth, other planets, and moons record ancient eruption conditions and thus hold key information about planetary thermal and chemical evolution and the creation of new crust (e.g., Zimbelman 1998; Hauber et al. 2009; Jaeger et al. 2010). On Earth, although lava flows represent a more localized hazard than explosive eruptions, they can result in significant damage to infrastructure and property (e.g., Behncke et al. 2005; Kauahikaua 2007; Crisci et al. 2008). Two important factors that control flow behavior (such as advance rate and maximum flow distance) are the lava effusion rate and the lava rheology (e.g., Walker 1973; Crisp et al. 1994; Pinkerton and Wilson 1994; Kilburn 2000; Harris and Rowland 2001). The instantaneous effusion rate, defined as the volume flux of erupted lava that is feeding a flow at a particular point in time (Lipman and Banks 1987), can be calculated by multiplying the average flow velocity by the cross-sectional lava flow area. When the flow is constrained within channels or tubes (Fig. 1), the area is often taken to be a simple multiplication of the visible flow width by its assumed depth, which inherently assumes a rectangular cross-section. Average flow velocity estimates can be made from measurements of flow surface velocity

Published online: 26 June 2014

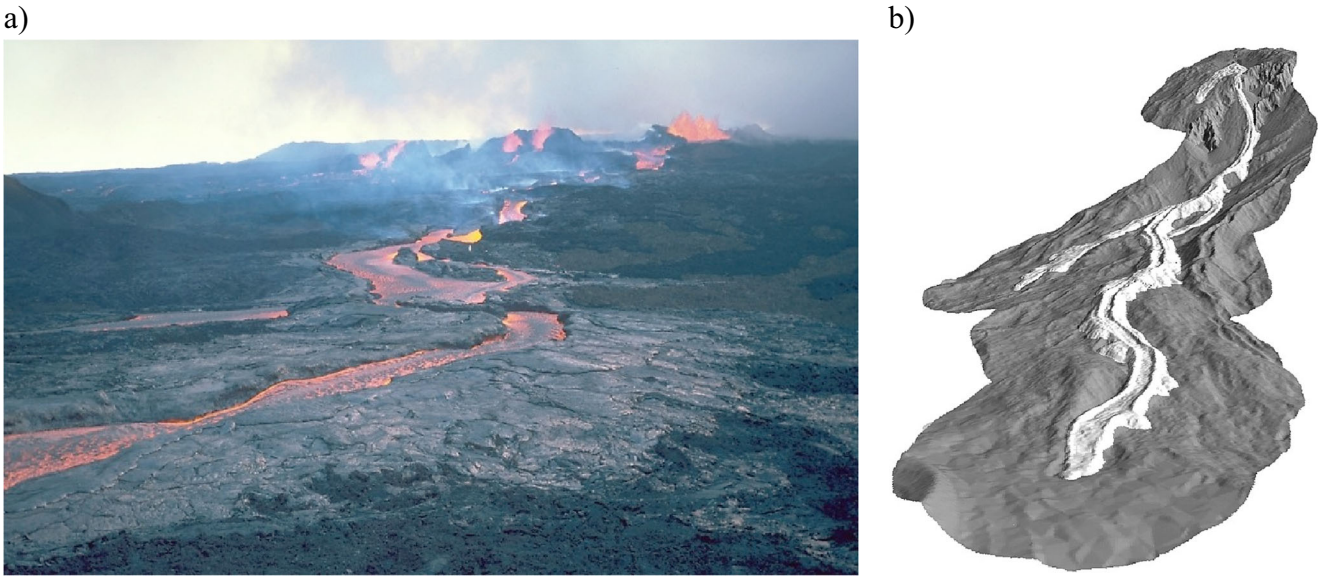

Fig. 1 Photos of lava flowing in channels. **a** Mauna Loa 1984. Photo taken by R.W. Decker. Source: USGS HVO website. **b** Etna 2004. A shaded relief 3D view of the laser scanning digital elevation model (DEM) made by Mazzarini et al. (2005). *Highlighted area* shows the September 2004 flow and channel. Illumination from the north

but such calculations also require knowledge of channel geometry and an assumption of the appropriate rheological model.

Lava, however, is a complex fluid, comprising of liquid melt, solid crystals, and gas bubbles, with volume ratios, number densities, and orientations all reflecting the flow history. Lava rheology depends on melt viscosity and the shape, distribution, and volume fraction of crystals and bubbles, all of which vary with the shear and thermal history over the duration and length of the flow. This complexity and time and space variability make it difficult to accurately apply rheological laws obtained in the laboratory or from theoretical calculations, to the bulk behavior of natural flows. Attempts have been made in the past to measure lava viscosity directly during flow emplacement, using viscometers (Shaw 1969; Pinkerton 1978); such direct measurements are extremely difficult to perform. In addition, point measurements provided by viscometers may not be representative of the effective bulk flow viscosity. For sample, they may use a strain-rate that is less than the characteristic strain rate of the flow (Spera et al. 1988). It is, therefore, valuable to be able to estimate the effective viscosity of flowing lava indirectly, whether in situ using observations of flow velocity and structure or from the geometry of solidified flows, in order to provide rheological information for predictions of flow advance, hazard mitigation, and geologic interpretation.

Early estimates of lava viscosity from velocity measurements were carried out for Etnean flows by Walker (1968). Hulme (1974) used measurements of flow velocity and dimensions to estimate viscosities of terrestrial lava flows. Fink and Zimbelman (1986) reported detailed measurements for four lava flows in Hawai'i and used them to estimate rheological parameters along the flow length. Similar calculations were carried out by Moore (1987), who estimated lava viscosity and yield stress for several Mauna Loa flows, finding values comparable to those measured in experiments. Advances in visible-light and infrared photography and videography in recent years allowed the scientists to make more detailed estimates of flow geometries, velocities, and temperature, and use those to infer flux and rheological parameters. For example, James et al. (2007) used infrared time-lapse photography of the September 2004 flow on Etna to estimate mass flux and rheology.

A common feature in all the above viscosity and flux estimations is the use of equations that assume a simplified channel geometry. The frequently used Jeffreys equation (Jeffreys 1925; Nichols 1939; Hulme 1974; Baloga et al. 1998) relates the viscosity η and the flux rate Q of a Newtonian fluid inside a channel to the lava density ρ, maximum velocity V, thickness h, half-width a, ground slope α, and gravitational acceleration g:

$$\eta = \frac{\rho g \sin(\alpha) h^2}{2V} \tag{1a}$$

$$Q = \frac{\rho g \sin(\alpha) h^3 2a}{3\eta} \tag{1b}$$

Jeffreys equation assumes a wide channel (i.e., much wider than it is deep), yet it is often used in scenarios where this assumption is not necessarily valid (see Table 1 for notation). Following Batchelor (1967), Tallarico and Dragoni (1999), Sakimoto and Gregg (2001), and others utilize a

Table 1 Notation and symbols used in the text

Symbol	Meaning	Units
a	flow half width	m
$\boldsymbol{f}$	body force	N/kg
g	gravitational acceleration	m/s^2
h	flow thickness, channel depth	m
m	power-law rheology exponent	
p	pressure	Pa
t	time	s
t_s	solidification time	s
K	V-shaped channel factor (Takagi and Huppert 2007)	
Q	volumetric flux tate	m^3/s
R	hydraulic radius	m
Ra	Rayleigh number	
Re	Reynolds number	
Pe	Pèclet number	
T	temperature	$^\circ K$
T_e	eruption temperature	$^\circ K$
T_a	ambient temperature	$^\circ K$
T_s	solidification temperature	$^\circ K$
u	velocity vector	m/s
V, V_{max}	velocity magnitude, maximum	m/s
α	ground slope	degrees
β, γ	geometrical factors in Eqs. 2 and 3	
δ	thermal boundary layer thickness	m
Γ	Gamma function	
ε	emissivity	
$\dot{\varepsilon}$	strain rate	1/s
η	viscosity	Pa s
Θ	non-dimensional temperature	
ϑ	flow and crust morphology parameter (Griffiths et al. 2003)	
κ	thermal diffusivity	m^2/s
λ_c	convective time scale	s
λ_r	radiative time scale	s
ρ	density	kg/m^3
σ	stress tensor	Pa
σ_b	Stephan-Boltzman constant	
Ψ	ratio of advection to solidification timescales	

formulation for velocity–viscosity relation for such finite-width rectangular channels:

$$\eta = \frac{\rho g \sin(\alpha) h^2}{2V} \times \beta \tag{2}$$

where $\beta = 1 - \frac{32}{\pi^5}\sum_{n=1,3,5,\ldots}^{\infty}\frac{1}{n^5}(-1)^{(n-1)/2}\mathrm{sech}\frac{n\pi 2a}{4\mathrm{h}}$. Hereafter, we refer to β as the "finite-width factor." The above studies examined the influence of assuming an infinitely-wide flow, a finite-width geometry, and a semi-elliptical geometry on the Newtonian and Bingham rheological parameters estimated from surface velocity and dimensions of both natural and laboratory flows, and found differences of up to 90 % for some flows. In addition, both Tallarico and Dragoni (1999) and Sakimoto and Gregg (2001) provide an expression for the mass flow rate in a rectangular channel given the channel dimensions and the lava's maximum surface velocity:

$$Q = \frac{4}{3} V a h \times \frac{\gamma}{\beta} \tag{3}$$

where $\gamma = 1 - \frac{384}{\pi^5}\sum_{n=1,3,5,\ldots}^{\infty}\frac{1}{n^5}\tanh\frac{n\pi 2a}{4\mathrm{h}}$. We call γ the "finite-width flux factor".

Moore (1987) used an equation for Newtonian flow in a semi-elliptical channel:

$$\eta = \frac{\rho g \sin(\alpha)}{V} \times \left\{ \frac{h^2}{2[(\frac{h}{a})^2 + 1]} + \frac{1}{2}[(\frac{h}{a})^2 + 1] \right\} \tag{4}$$

We note that Moore (1987) based this work on a more general relationship applicable also to Bingham fluids (Johnson 1970). Although the generalization was later found to be erroneous (Johnson and Rodine 1984), the Newtonian variant (Eq. 4) is correct. Robertson and Kerr (2012a) provide a detailed method for estimating the rheological parameters of a Bingham fluid given the maximum velocity and the flow depth or rate. Their method is based on iteratively searching for a numerically-calculated velocity which provides the best fit to the observed velocity. Like most others, their work assumed a rectangular channel cross-section.

Takagi and Huppert (2007) expanded the range of considered channel shapes by employing similarity solutions to investigate the influence of confining boundaries on viscous flows driven by gravity. They looked at semi-circular ($a = h$) and V-shaped channels, and provided analytical expressions for flow velocity–viscosity relation depending on channel shape. Following the formulation of Eqs. 1a–4, Takagi and Huppert (2007) defined $\eta = \rho g \sin(\alpha) h^2 / V \times K$, where K depends on the V-shape opening angle or the semi-circle curvature ($K = \frac{1}{2}$ yields the Jeffreys equation). For a V-shape channel, $K \approx \frac{0.137(a/h)^3}{1+(a/h)^2}$, and for a semi-circular channel, $K = \frac{24}{105} = 0.23$.

Our goal here is to build upon these past works and further expand the discussion of the influence of channel shape on flow observable to include more complex channel geometries. This will enable us to provide a range of possible solutions to bracket field estimates of viscosity and flux when channel geometry is poorly constrained. Our approach is to carry out numerical simulations of flows in a variety of

channel geometries and determine the viscosity values that would be estimated in the field from surface measurements alone, using the equations above. We consider Newtonian and non-Newtonian fluid rheologies, including isothermal and non-isothermal cases.

Methods

We constructed a suite of finite element numerical models with varying rheologies and channel geometries to assess the influence of channel shape on the rheological and flux parameters inferred from observed surface velocities. We assumed a steady-state, laminar flow, and solved for the instantaneous velocity field for different geometry, rheology, and temperature combinations. For all models, lava density was set to 2,400 kg/m^3, and ground slope is assumed to be 33 degrees for all models. The flow is controlled by the equation of conservation of momentum:

$$\rho\left(\frac{\partial \mathbf{u}}{\partial t} + (\mathbf{u}\cdot\nabla)\mathbf{u}\right) - \nabla\cdot\sigma = \rho\boldsymbol{f} \tag{5}$$

and the equation of continuity for an incompressible fluid:

$$\nabla\cdot\mathbf{u} = 0 \tag{6}$$

where $\mathbf{u}$ is the velocity vector, σ is the stress tensor, and $\boldsymbol{f}$ a body force. We assume a steady-state, which implies that $\frac{\partial \mathbf{u}}{\partial t} = 0$.

To solve the flow equations, we use the open-source finite element package ELMER, developed at the Center for Scientific Computing, Finland (http://www.csc.fi/elmer/). The system of equations was solved iteratively using the biconjugate gradient stabilized method (e.g., Barrett et al. 1994, p.24–25), with ILU(2) (Incomplete LU factorization of level 2) preconditioning to promote convergence. Flows were driven by an applied gravitational body force equal to $\rho g \sin(\alpha)$, and we applied no-slip boundary conditions ($\mathbf{u} = 0$) at the bottom and side walls of each channel. Flow at the surface was unconstrained and could move in any direction. Meshes were refined near boundaries and tested to ensure the solution was independent of mesh resolution (i.e., solutions did not change with further mesh refinement) while balancing computational cost. The accuracy of the solutions calculated by ELMER could be assessed by comparing the numerical results with equivalent analytical solutions where available. Supplementary material Fig. S1 shows the results from such comparison for a rectangular and a semi-elliptical channels using Eqs. 2 and 4.

Channel geometries

A total of 13 different channel geometries were considered (Table 2, Fig. 2), 8 of which were straightforward geometric shapes, not intended to accurately represent natural channels, but to cover geometrical end-members:

- two rectangular open channels, one 'shallow,' and one 'deep' (models 1 and 2)
- three semi-elliptical open channels of varying aspect ratios (models 3, 4, and 5)
- a truncated elliptical channel (i.e., partially-filled tube or a channel with levees starting to converge towards the surface) (model 6)
- a V-shaped open channel (model 7)
- a trapezoid open channel (model 8)

For simplicity, we keep our models dimensional and ascribe a width of 1 m to all geometric channels, to maximize similarity. The truncated elliptical channel (tube-like) is truncated at 5/6 of its height and has the same minor axis length as the medium semi-elliptical model. Nonetheless, the results give intuition for behavior in channels of different sizes, through examining the channel aspect ratio (width/depth) and departure from a rectangular or semi-elliptical shape.

The remaining five models were derived from field data on the

- two cross-sections from the Mauna Loa 1984 flow, Hawai'i, taken at altitudes of (A) 2,333 m and (B) 2,198 m (models 9 and 10)
- three cross-sections from the September 2004 flow on Mount Etna, Sicily, taken at altitudes of (A) 1,729 m, (B) 1,723 m, and (C) 1,719 m (models 11,12, and 13)

Channel structure for the Mauna Loa 1984 flow was extracted from an airborne LiDAR data collected over the flow area in June 2009 (data are publicly available via NSF's OpenTopography portal). Channel geometries for the Etna 2004 flow were derived from the photogrammetric survey of James et al. (2007) which imaged the channel under conditions of near complete drainage.

Rheological models

Within the above channels, flows with three different rheological constitutive laws were considered:

- a Newtonian viscosity fluid
- a power-law viscosity fluid defined as $\eta = \eta_0\dot{\varepsilon}^{m-1}$, with $\dot{\varepsilon}$ the strain rate. We use an exponent of $m = 0.6$, following laboratory estimates for basaltic lavas (e.g., Sonder et al. 2006), and

Table 2 Geometry information for all channel models used

Model number	Shape	Width (m)	Depth (m)	Actual Cross-sectional area (m^2)	Wetted perimeter (m)	Hydraulic radius (m)	Finite-width factor β	Finite-width flux factor γ	Solidification time t_s (s)	Deviation from rectangular
1	Rectangle deep	1.00	0.80	0.80	2.60	0.31	0.33	0.24	67	0.00
2	Rectangle - shallow	1.00	0.40	0.40	1.80	0.22	0.72	0.52	67	0.00
3	Half-ellipse - shallow	1.00	0.25	0.20	2.48	0.08	0.91	0.69	67	0.21
4	Half-ellipse - medium	1.00	0.50	0.39	3.14	0.13	0.59	0.42	67	0.21
5	Half-ellipse - deep	1.00	0.80	0.63	4.19	0.15	0.33	0.24	67	0.21
6	V	1.00	0.50	0.25	1.41	0.18	0.59	0.42	67	0.50
7	Trapezoid	1.00	0.40	0.30	1.44	0.21	0.72	0.52	67	0.25
8	Tube	1.00	0.60	0.52	1.96	0.27	0.48	0.35	67	0.13
9	Mauna Loa A	23.30	2.30	40.27	26.65	1.51	1.00	0.88	67	0.25
10	Mauna Loa B	12.30	4.60	33.90	15.59	2.17	0.75	0.54	67	0.40
11	Etna A	5.60	2.12	7.35	6.22	1.18	0.75	0.54	67	0.38
12	Etna B	4.54	0.69	2.03	4.57	0.44	0.99	0.81	67	0.35
13	Etna C	5.72	1.09	3.15	6.01	6.01	0.97	0.76	67	0.49

- a temperature-dependent Newtonian viscosity fluid, with viscosity defined as $log_{10}(\eta_0) = -A + B/(T - C)$ (Fulcher 1925). We set the parameters A, B, and C using the values that the GRD model (Giordano et al. 2008) predicts for the composition of the Etna 2004 flows: A = 4.55, B = 5596, and C = 499.

This approach to temperature-dependent viscosity was aimed at illustrating first-order temperature effects on bulk rheology, but neglects complexities such as crystals fraction variability, which can have significant effects down flow (e.g., Chevrel et al. 2013). For the natural channels (models 9–13), we multiply the pure-melt viscosity calculated by the GRD model by a factor of 30. This factor accounts for the higher viscosity expected due to approximately 30 % bubbles and 40 % crystal fraction (Harris and Allen 2008), and elevates the effective viscosities in these models to levels comparable to those measured in the field (Lipman and Banks 1987; James et al. 2007).

For models with a temperature-dependent viscosity, we imposed a temperature field within the channel to be used by the viscosity law. The temperature field was calculated in advance for each channel geometry by solving the equation of heat conduction within the fluid, assuming an initial temperature of $T_e = 1,100$ ° C and an upper surface boundary of 900 °C (i.e., temperatures similar to those measured at Etna in 2001 by Bailey et al. (2006) using thermocouples). The fluid cooled by radiation from the free surface (using an emissivity value of $\varepsilon = 0.95$ (Patrick et al. 2004)) and through conduction to the solid boundary (using a thermal diffusivity $\kappa = 5 \times 10^{-7}$ m^2/s for both the fluid and the channel, and a fixed temperature of $T_a = 300$ °C for the channel wall material).

We ran the cooling model for 1,000 s, by which time the top thermal boundary layer reached a thickness $\delta = 10$ cm for all geometries.This is a relatively thick thermal boundary layer—~2.5 times that expected by considering the Rayleigh number (R_a) of the flow and using the theoretical relationship $\delta = 1.7hRa^{-\frac{1}{3}}$, and $Ra = \rho g \alpha (T_e - T_s)h^3/\kappa\eta$. However, flows with thinner thermal boundary layers will be increasingly well approximated by the isothermal case. Therefore, our models can be thought of as end member scenarios for the effect of thermal structure and temperature-dependent rheology. Vertical profiles of temperature taken at each channel's center are shown in Fig. 3a. The simple nature of the cooling model, which neglects any heat advection due to down-flow shear or across-flow velocity components, limits analysis to first-order thermal effects. Nevertheless, this represents a reasonable starting place for examining the effects of a temperature-dependent rheology, with the 900–1,100 °C range giving viscosities of 5,660–71 Pa/s (models 1–8) and 7.2×10^4–1,770 Pa/s (models 9–13) at the flows' surface and interior, respectively.

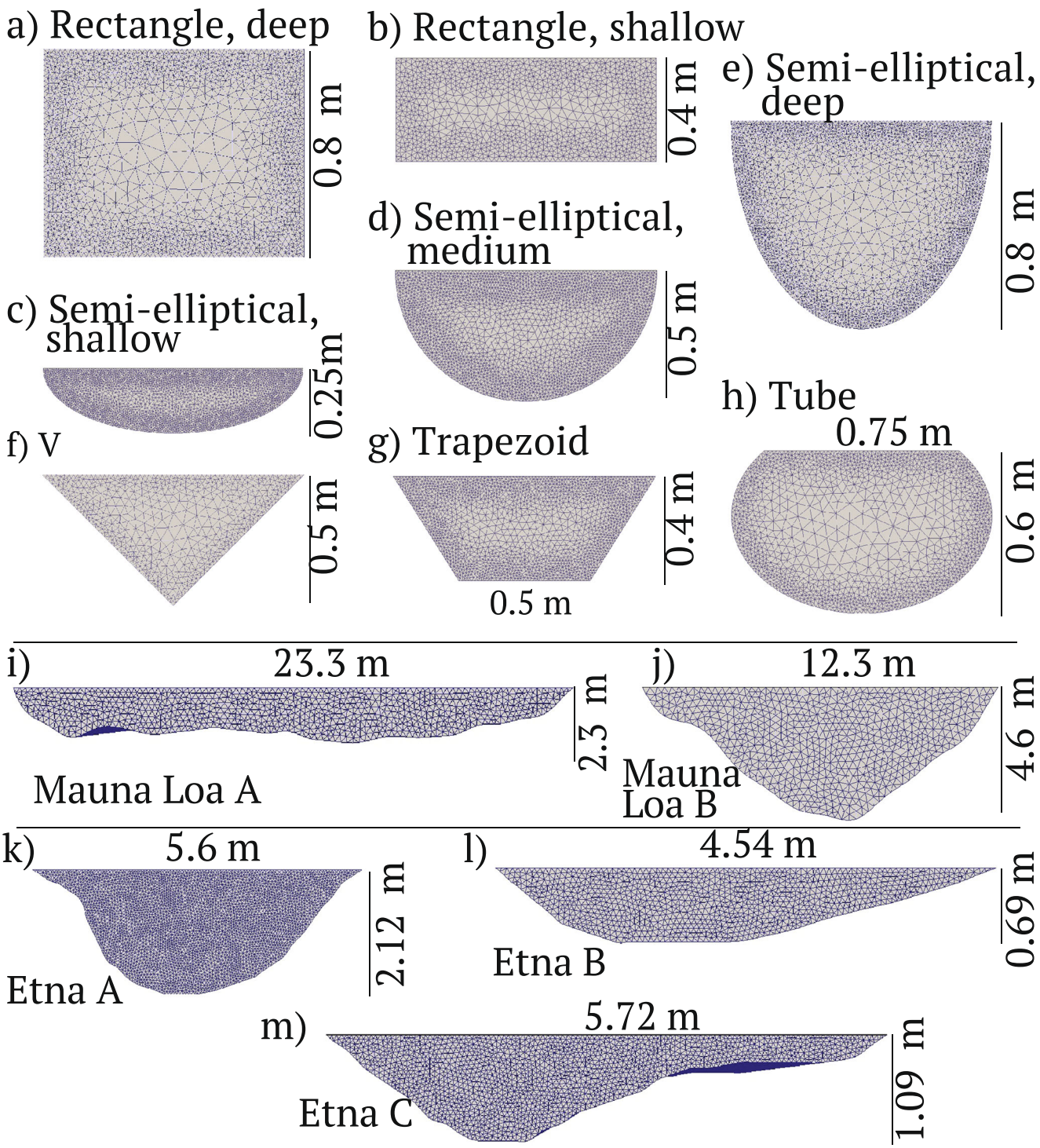

Fig. 2 Geometries used for numerical forward models. **a–h** Geometrical shapes of models 1–8 (width is always 1 m): **a** A *narrow rectangular channel* (also used for testing against analytical solution); **b** A *shallow rectangular channel*. **c–e** *Semi-elliptical channels*, width depths of 0.25, 0.375, and 0.8 m; **f** A *V-shaped channel* with a depth of 0.5m; **g** A *trapezoid channel*, width a depth of 0.4m. **h** A partially-filled elliptical tube with a minor axis radius of 0.375 m; **i-j** Cross-sections from the Mauna Loa 1984 flow, extracted from LiDAR data by Hannah Dietriech. **k–m** Cross-sections from the Etna 2004 flow, taken from James et al. (2007)

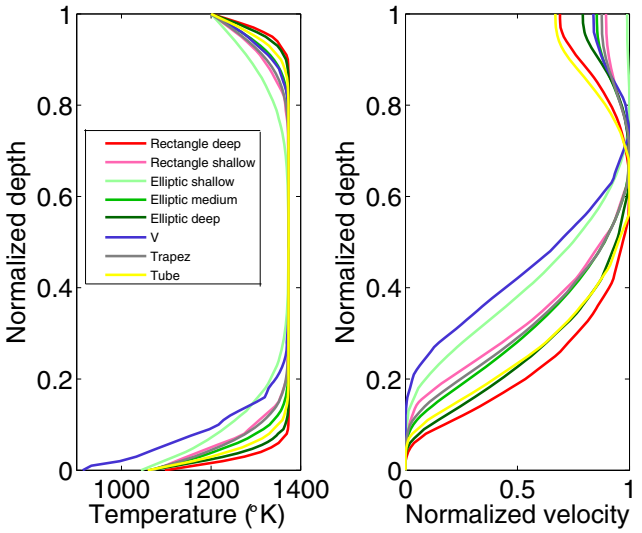

Fig. 3 Vertical cross-sections at the center of each channel of the **a** temperature and **b** velocity for models with a temperature-dependent viscosity. The velocities are normalized by each model's maximum velocity and the depth are normalized by the thickness of the channel

Post-processing procedure

We calculate the viscosities that an observer would calculate for the flowing lava given its surface velocity, the modeled channel height and width, and assuming either the Jeffreys equation (Eq. 1a), a finite-width rectangular channel (Eq. 2), or a semi-elliptical geometry (Eq. 4) and the same flow thickness h used in the numerical simulation. For Eqs. 2 and 4, the half-width a is that used in the numerical model as well. For models with power-law rheology, we report an effective input viscosity value calculated as $\eta = \eta_0 \dot{\varepsilon}^{m-1}$, where $\dot{\varepsilon}$ is an average strain rate magnitude in the model, η_0 is a reference viscosity, and $m = 0.6$. For temperature-dependent viscosity models, we estimated an effective input viscosity for the lava in each model by taking the geometric mean of the viscosities at n equally distributed nodes along a vertical slice through the channel $\left(\left(\prod_{i=1}^{n} \eta_i\right)^{\frac{1}{n}}\right)$.

We quantify the error introduced to viscosity and flux estimations when assuming an inappropriate channel geometry by reporting the ratios between the viscosity calculated using the simplified analytical relationships (Eqs. 1a, 2 and 4), and the actual effective viscosity used as input in the numerical forward models. For each model, we also calculate the "misfit" value, defined as $(1-\frac{inferred}{input})^2$. In addition to viscosities, we also compare flux estimations an observer would make using Eqs. 1b and 3 with the simulated fluxes in the channel.

Applicability to natural channels

For simplicity, our models were constructed using specific channel dimensions, yet their broader applicability can be illustrated through the non-dimensional parameters Re (Reynolds number), Pe (Péclet number) Ψ (Fink and Griffiths 1990), and ϑ (Griffiths et al. 2003), as given in Tables 3, 4 and 5.

The Reynolds number Re expresses the relative significance between inertial forces and viscous forces. For an open channel, Re is defined as $\frac{\rho R V}{\eta}$, where R is the hydraulic radius of the flow, which is the ratio of the cross-section area to the length of the flow's wetted perimeter. For a half-circle channel, the hydraulic radius equals half the channel depth. Flow in an open channel is considered laminar for Re <500 and turbulent for Re >2,000. We find that all the flows in our models are clearly laminar, with $Re << 500$. The Péclet number Pe gives the ratio of advection to diffusion of heat, and a measure of the relative thickness of the thermal boundary layer to the characteristic length scale. All Péclet numbers in our models are much greater than 1, meaning that advection dominates.

The non-dimensional parameter Ψ represents the ratio between the amount of time required for a crust to form at the flow surface (t_s) and the time it takes to advect heat to a distance equivalent to the flow depth, calculated as the maximum velocity divided by the depth (Fink and Griffiths 1990; Gregg and Fink 2000; Gregg and Keszthelyi 2004). Ψ values have been found to correlate with flow morphologies in both field and laboratory scenarios (Fink and Griffiths 1990; Gregg and Keszthelyi 2004): high Ψ values correspond to more disrupted flow structures and surfaces, with $\Psi > 30$ corresponding to leveed flows and $\Psi > 9$ to cracked and broken lava toes. Low Ψ values correlate with tube formation and inflated toes. We calculate Ψ values using the following set of equations and definitions (Robertson and Kerr 2012b):

$$
\begin{aligned}
\Psi &= \frac{V_{max}}{h} \times t_s \\
t_s &= \frac{\lambda_c}{2} \times \left[\frac{1-\Theta_s+\Theta_a}{(\Theta_s-\Theta_a)^{\frac{4}{3}}+\Lambda^{\frac{1}{2}}(\Theta_s^4-\Theta_a^4)} \right] \\
\Lambda &= \frac{\lambda_c}{\lambda_r}\lambda_c = \left(\frac{\rho c}{\rho_a c_a J_a}\right)^2 \frac{\kappa}{(T_e-T_a)^{\frac{2}{3}}} \\
\lambda_r &= \left(\frac{\rho c}{\varepsilon \sigma_b}\right)^2 \frac{\kappa}{(T_e-T_a)^6} \\
J_a &= 0.1\left(\frac{g\rho_a\alpha_a\kappa_a^2}{\eta_a}\right)^{\frac{1}{3}}
\end{aligned}
\qquad (7)
$$

where the subscript a refers to the properties of the ambient air, subscript e refers to eruption conditions, and subscript s to solidification conditions. θ_s, θ_a, and θ_e are non-dimensional temperatures formed by dividing by $(T_e - E_a)$, i.e., $\theta_s = T_s/(T_e - T_a)$. The solidification time t_s

Table 3 Summary of model parameters and results – Newtonian isoviscous models

Model number	Shape	Input viscosity (Pa s)	Maximum surface velocity (m/s)	Measured flux (m^3/s)	Reynolds number	Pèclet number	Ψ	Rayleigh Number	ϑ
1	Rectangle - deep	1200	1.11	0.43	0.68	$1.8x10^6$	92.96	1.49×10^7	4923
2	Rectangle - shallow	1200	0.61	0.12	0.27	4.9×10^5	102.18	1.86×10^6	2705
3	Half-ellipse - shallow	1200	0.27	0.03	0.04	1.3×10^5	71.29	4.53×10^5	1180
4	Half-ellipse - medium	1200	0.68	0.13	0.17	6.8×10^5	91.12	3.63×10^6	3016
5	Half-ellipse - deep	1200	0.96	0.31	0.29	1.5×10^6	80.65	1.49×10^7	4271
6	V	1200	0.39	0.05	0.14	3.9×10^5	52.26	3.63×10^6	1730
7	Trapezoid	1200	0.51	0.07	0.21	4.1×10^5	85.43	1.86×10^6	2262
8	Tube	1200	0.80	0.21	0.43	9.6×10^5	89.33	6.27×10^6	3548
9	Mauna Loa A	12000	2.36	45.38	0.71	1.1×10^7	28.67	5.17×10^5	496
10	Mauna Loa B	12000	5.64	89.50	2.45	5.2×10^7	34.25	4.14×10^6	1185
11	Etna A	100000	0.16	0.57	0.00	7.0×10^5	0.40	4.05×10^5	699
12	Etna B	50000	0.03	0.03	0.00	3.7×10^4	1.62	1.40×10^4	111
13	Etna C	50000	0.09	0.12	0.03	2.1×10^5	0.26	5.51×10^4	200

Model number	Shape	Inferred viscosity Jeffreys	Inferred/ Input ratio	Misfit (1-inferred/ input)^2	Inferred viscosity finite-width rectangle	Inferred/ Input ratio	Misfit (1-inferred/ Input)^2	Inferred viscosity semi-elliptical	Inferred/ Input ratio	Misfit (1-inferred/ input)^2	Estimated flux(m^3/s) - Jeffreys	Estimated/ Measured flux ratio	Misfit (1-inferred/ input)^2	Estimated flux(m^3/s) - Finite-width	Estimated/ Measured flux ratio	Misfit (1-inferred/ input)^2	Difference in analytical flux predictions
1	Rectangle - deep	3693	3.08	4.32	1203	1.00	0.00	1037	0.86	0.02	1.18	2.73	2.99	0.43	1.00	0.00	2.99
2	Rectangle - shallow	1680	1.40	0.16	1203	1.00	0.00	1024	0.85	0.02	0.33	2.71	2.93	0.12	0.98	0.00	2.93
3	Half-ellipse - shallow	1505	1.25	0.06	1371	1.14	0.02	1204	1.00	0.00	0.09	2.96	3.82	0.03	1.11	0.01	3.81
4	Half-ellipse - medium	2355	1.96	0.93	1387	1.16	0.02	1177	0.98	0.00	0.45	3.49	6.19	0.16	1.25	0.06	6.12
5	Half-ellipse - deep	4257	3.55	6.49	1387	1.16	0.02	1196	1.00	0.00	1.03	3.31	5.35	0.38	1.21	0.05	5.31
6	V	4106	3.42	5.86	2420	2.02	1.03	2053	1.71	0.51	0.26	5.20	17.64	0.09	1.86	0.74	16.90
7	Trapezoid	2009	1.67	0.45	1439	1.20	0.04	1225	1.02	0.00	0.27	3.89	8.33	0.10	1.40	0.16	8.17
8	Tube	2882	2.40	1.97	1389	1.16	0.02	1181	0.98	0.00	0.64	3.05	4.19	0.23	1.09	0.01	4.18
9	Mauna Loa A	14357	1.20	0.04	14357	1.20	0.04	13818	1.15	0.02	7.24	0.16	0.71	3.17	0.07	0.87	-0.16
10	Mauna Loa B	24030	2.00	1.00	18022	1.50	0.25	15409	1.28	0.08	34.59	0.39	0.38	12.52	0.14	0.74	-0.36
11	Etna A	180217	1.80	0.64	131645	1.32	0.10	111569	1.12	0.01	0.46	0.81	0.04	0.17	0.29	0.51	-0.47
12	Etna B	117262	2.35	1.81	113068	2.26	1.59	104550	2.09	1.19	0.02	0.97	0.00	0.01	0.39	0.37	-0.37
13	Etna C	82591	1.65	0.42	78028	1.56	0.31	70239	1.40	0.16	0.14	1.11	0.01	0.05	0.43	0.32	-0.31
Total misfit				4.9153			1.8608			1.4203			7.2505			1.9559	

Top: Flow results measured directly from models (velocity and flux); Bottom: Inferred viscosity and flux using the different analytical solutions discussed in the text. Background colors identify segments based on the same equation. The values in the bottom row give an overall misfit sum for the segment/equation, calculated as $[\sum(1 - \frac{inferred}{input})^2]^{\frac{1}{2}}$. First, three results segment on the left deal with viscosity estimates, and the right two segments handle flux estimates. The rightmost column shows the difference in misfit values produced by flux estimations using Eqs. 1b and 3. When the difference is greater than zero, Eq. 3 gives a better fit and when difference < 0 – Eq. 1b is better

Table 4 Summary of model parameters and observations—Power-law rheology models

Model number	Shape	Maximum velocity (m/s)	Measured flux (m^2/s)	Average strain rate (1/s)	Reference viscosity (Pa s)	Effective viscosity (Pa s)	Reynolds number	Pèclet number	Ψ	Rayleigh Number	ϑ
1	Rectangle - deep	10.70	6.90	30.67	120	3.1×10^1	259.04	1.7×10^7	897	1.49×10^8	102285
2	Rectangle - shallow	7.36	2.19	27.05	120	3.2×10^1	122.28	5.9×10^6	1232	1.86×10^7	70294
3	Half-ellipse - shallow	5.76	0.75	28.31	120	3.2×10^1	34.67	2.9×10^6	1543	4.53×10^6	55009
4	Half-ellipse - medium	7.71	2.41	27.09	120	3.2×10^1	72.13	7.7×10^6	1033	3.63×10^7	73672
5	Half-ellipse - deep	8.58	4.52	26.58	120	3.2×10^1	95.59	1.4×10^7	719	1.49×10^8	82030
6	V	6.33	1.07	26.58	120	3.2×10^1	83.12	6.3×10^6	848	3.63×10^7	60491
7	Trapezoid	6.93	1.53	27.24	120	3.2×10^1	107.97	5.5×10^6	1160	1.86×10^7	66171
8	Tube	8.00	3.38	26.43	120	3.2×10^1	158.93	9.6×10^6	894	6.27×10^7	76470
9	Mauna Loa A	10.34	203.77	3.66	5000	3.0×10^3	12.61	4.8×10^7	126	5.04×10^7	10019
10	Mauna Loa B	12.64	250.38	4.00	5000	2.9×10^3	22.97	1.2×10^8	77	4.03×10^8	12244
11	Etna A	6.94	33.30	5.06	1200	6.3×10^2	31.38	2.9×10^7	92	1.64×10^8	10817
12	Etna B	4.47	4.64	6.09	1200	5.8×10^2	8.18	6.2×10^6	181	5.67×10^6	6959
13	Etna C	5.94	8.94	5.98	1200	5.9×10^2	145.94	1.3×10^7	153	2.23×10^7	9258

Model number	Shape	Inferred viscosity Jeffreys	Inferred/ Input ratio	Misfit (1-inferred/ input)^2	Inferred viscosity finite-width rectangle	Inferred/ Input ratio	Misfit (1-inferred/ Input)^2	Inferred viscosity semi-elliptical	Inferred/ Input ratio	Misfit (1-inferred/ input)^2	Estimated flux(m^3/s) - Jeffreys	Estimated/ Measured flux ratio	Misfit (1-inferred/ input)^2	Estimated flux(m^3/s) - Finite-width	Estimated/ Measured flux ratio	Misfit (1-inferred/ input)^2	Difference in analytical flux predictions
1	Rectangle - deep	383	12.55	133.38	125	4.09	9.54	108	3.52	6.38	11.42	1.65	0.43	4.18	0.61	0.15	0.27
2	Rectangle - shallow	139	4.34	11.17	100	3.11	4.45	85	2.65	2.71	3.92	1.79	0.62	1.41	0.64	0.13	0.50
3	Half-ellipse - shallow	70	2.21	1.46	63	2.01	1.02	56	1.77	0.59	1.92	2.56	2.44	0.72	0.96	0.00	2.44
4	Half-ellipse - medium	208	6.48	29.99	122	3.81	7.92	104	3.24	5.01	5.14	2.14	1.29	1.84	0.76	0.06	1.23
5	Half-ellipse - deep	477	14.78	189.83	156	4.81	14.55	134	4.15	9.93	9.16	2.03	1.05	3.36	0.74	0.07	0.99
6	V	253	7.83	46.62	149	4.61	13.06	126	3.91	8.49	4.22	3.94	8.66	1.51	1.41	0.17	8.49
7	Trapezoid	148	4.63	13.14	106	3.31	5.35	90	2.82	3.31	3.69	2.41	1.99	1.33	0.87	0.02	1.97
8	Tube	288	8.90	62.35	139	4.29	10.81	118	3.65	7.00	6.40	1.90	0.80	2.30	0.68	0.10	0.70
9	Mauna Loa A	3276	1.10	0.01	3276	1.10	0.01	3153	1.06	0.00	31.72	0.16	0.71	323.72	1.59	0.35	0.37
10	Mauna Loa B	10722	3.73	7.47	8041	2.80	3.241	6876	2.39	1.94	77.53	0.31	0.48	345.21	1.38	0.14	0.33
11	Etna A	4148	6.61	31.50	3111	4.96	15.68	2637	4.20	10.27	19.62	0.59	0.17	39.40	1.18	0.03	0.14
12	Etna B	683	1.17	0.03	676	1.16	0.03	626	1.07	0.01	4.11	0.89	0.01	7.61	1.64	0.41	-0.40
13	Etna C	1281	2.18	1.40	1243	2.12	1.25	1119	1.91	0.82	8.63	0.97	0.00	19.34	2.16	1.35	-1.35
Total misfit				22.99			9.32			7.51			4.32			1.73	

Table structure and formatting are the same as for Table 3

Table 5 Model parameters and results for models with temperature-dependent viscosity

Model number	Shape	Max interior velocity (m/s)	Max surface velocity (m/s)	Measured flux (m^3/s)	Effective viscosity (Pa s)	Reynolds number	Pèclet number	Ψ	Rayleigh number	ϑ
1	Rectangle - deep	6.77	4.67	2.58	91	55	1.1×10^7	391	6.91×10^9	160342
2	Rectangle - shallow	3.41	3.05	0.58	142	13	2.7×10^6	511	3.87×10^9	172880
3	Half-ellipse - shallow	1.69	1.67	0.13	208	2	8.4×10^5	448	4.09×10^9	154466
4	Half-ellipse - medium	4.27	3.65	0.76	122	10	4.3×10^6	489	5.75×10^9	188764
5	Half-ellipse - deep	5.46	4.33	1.69	100	20	8.7×10^6	362	1.05×10^{10}	171080
6	V	2.30	1.93	0.22	236	4	2.3×10^6	259	1.98×10^{10}	150913
7	Trapezoid	3.26	2.86	0.42	136	12	2.6×10^6	479	5.30×10^9	179730
8	Tube	4.75	3.18	1.12	110	28	5.7×10^6	355	6.73×10^9	144272
9	Mauna Loa A	4.00	4.00	70.20	12467	1	1.8×10^7	49	3.59×10^9	16060
10	Mauna Loa B	11.94	11.55	215.08	3055	20	1.1×10^8	70	9.37×10^9	31928
11	Etna A	3.64	3.60	12.75	86	120	1.5×10^7	134	1.55×10^{10}	13189
12	Etna B	6.89	6.87	7.02	124	59	9.5×10^6	787	9.68×10^8	22282
13	Etna C	7.93	7.24	12.59	128	890	1.7×10^7	525	2.13×10^9	23234

Model number	Shape	Inferred viscosity Jeffreys	Inferred/ Input ratio	Misfit (1-inferred/ input)^2	Inferred viscosity finite-width rectangle	Inferred/ Input ratio	Misfit (1-inferred/ Input)^2	Inferred viscosity semi-elliptical	Inferred/ Input ratio	Misfit (1-inferred/ input)^2	Estimated flux(m^3/s) - Jeffreys	Estimated/ Measured flux ratio	Misfit (1-inferred/ input)^2	Estimated flux(m^3/s) - Finite-width	Estimated/ Measured flux ratio	Misfit (1-inferred/ input)^2	Difference in analytical flux predictions
1	Rectangle - deep	878	8.20	51.79	286	2.67	2.79	247	2.30	1.70	7.22	2.82	3.29	2.64	1.03	0.00	3.29
2	Rectangle - shallow	336	2.38	1.91	241	1.71	0.50	205	1.45	0.20	1.82	3.18	4.75	0.65	1.14	0.02	4.73
3	Half-ellipse - shallow	239	1.68	0.46	218	1.53	0.28	191	1.34	0.12	0.56	4.26	10.63	0.21	1.60	0.37	10.27
4	Half-ellipse - medium	439	3.16	4.65	258	1.86	0.74	219	1.58	0.33	2.85	3.77	7.65	1.02	1.35	0.12	7.53
5	Half-ellipse - deep	948	7.23	38.86	309	2.36	1.84	266	2.03	1.06	5.83	3.47	6.09	2.14	1.27	0.07	6.02
6	V	829	4.85	14.79	488	2.86	3.45	414	2.42	2.03	1.54	7.03	36.40	0.55	2.52	2.30	34.10
7	Trapezoid	359	2.53	2.35	257	1.81	0.66	219	1.54	0.30	1.74	4.16	9.99	0.63	1.50	0.25	9.75
8	Tube	726	7.04	36.44	350	3.39	5.72	298	2.88	3.55	3.80	3.42	5.87	1.36	1.23	0.05	5.82
9	Mauna Loa A	8471	0.51	0.24	8471	0.51	0.24	8153	0.50	0.25	12.27	0.17	0.68	5.38	0.08	0.85	-0.17
10	Mauna Loa B	11734	0.82	0.03	8801	0.62	0.15	7525	0.53	0.22	73.23	0.34	0.43	26.51	0.12	0.77	-0.33
11	Etna A	5960	1.96	0.92	4470	1.47	0.22	3789	1.25	0.06	13.90	0.80	0.04	4.99	0.29	0.51	-0.47
12	Etna B	4089	0.73	0.07	4048	0.72	0.08	3744	0.67	0.11	0.68	1.04	0.00	0.28	0.42	0.33	-0.33
13	Etna C	5663	1.15	0.02	5493	1.12	0.01	4945	1.00	0.00	1.98	1.13	0.02	0.78	0.44	0.31	-0.30
Total misfit				12.30			4.00			3.05			9.20			1.78	

Model input conditions for all geometries were a surface temperature of 900 °C and a maximum interior temperature of 1,100 °C, which imply viscosities of 5,660-71 Pa/s (models 1–8) and 7.2 $\times 10^4$-1,770 Pa/s (models 9–13) at the flows' surface and interior, respectively. Table structure and formatting are the same as in Table 3

is 67 s for the temperatures used in our geometrically shaped models ($T_e = 1100$ °C, $T_a = 20$ °C, and $T_s = 730$ °C). Ψ values for all our models are in the high-Ψ, broken-surface regime, supporting our examination of them as open channels. A related characterization is given by Griffiths et al. (2003), who define the parameter $\vartheta = \Psi(R_a/R_0)^{\frac{1}{3}}$, where R_a is the Rayleigh number, and we take R_0 to be equal to 100. $\vartheta < 25$ indicates a likely development of a solid roof and a tube regime, while $\vartheta > 25$ leads to a mobile crust and an open channel flow. For all our models, $\vartheta > 25$, thus they are all within the mobile crust regime.

Results

We summarize our observations in Tables 3, 4, and 5, which list the measured velocities and flux rates for all our forward models, the derived non-dimensional parameters, and the results of the comparison with analytical predictions. Figure 4 shows cross-sections in the velocity fields across the geometrical channels.

Apparent viscosity and flux for isothermal models

Our results for the isothermal, Newtonian rectangular, and semi-elliptical channels agree with those predicted by the respective analytical solutions (Eqs. 2 and 4), confirming the validity of the numerical solution.

For Newtonian isoviscous models, the ratio of inferred viscosity to input viscosity ranges between 1.17 and 3.55, both occurring when using the Jeffreys equation. Considering a rectangular channel with a finite width leads to overestimations up to 102 % (ratio of 2.02). Using Eq. 4 (semi-elliptical) gives ratios of between 0.85 and 1.71.

We note that two of our numerical flow solutions—namely for V-shaped and medium-depth semi-elliptical channels—disagree with predictions made by the analytical solution of Takagi and Huppert (2007), using the equations we listed at the end of Section "Introduction." For a V-shaped channel, Takagi and Huppert (2007) predict a factor $K = 0.0685$, giving $V_{max} = 0.24$ m/s, compared with our measured 0.39 m/s. For a medium-depth semi-circular channel, Takagi and Huppert (2007) use a factor of $24/105 = 0.229$, leading to a maximum velocity of 0.8 m/s, 17 % greater than both the analytical solution by Moore (1987) and our numerical solution (0.68 m/s).

To estimate the influence of channel shape assumptions when a power-law rheology is used, we first have to calculate the effective viscosity of the model by finding the highest strain rate within the channel and using it in the constitutive relation described in the Methods section. Our results indicate that the inferred viscosity can be up to 3.7 times larger than the effective viscosity (using the Jeffreys equation for a deep and narrow semi-elliptical channel), and down to a factor of 0.30 (the Jeffreys equation for a shallow semi-elliptical channel).

Temperature-dependent models

Figure 3 shows vertical cross-sections of the temperature and the velocity magnitude taken at the center of each channel. Table 5 lists the observed maximum velocities at the channel surface and in the interior, along with the viscosities inferred from these velocities assuming a finite-width

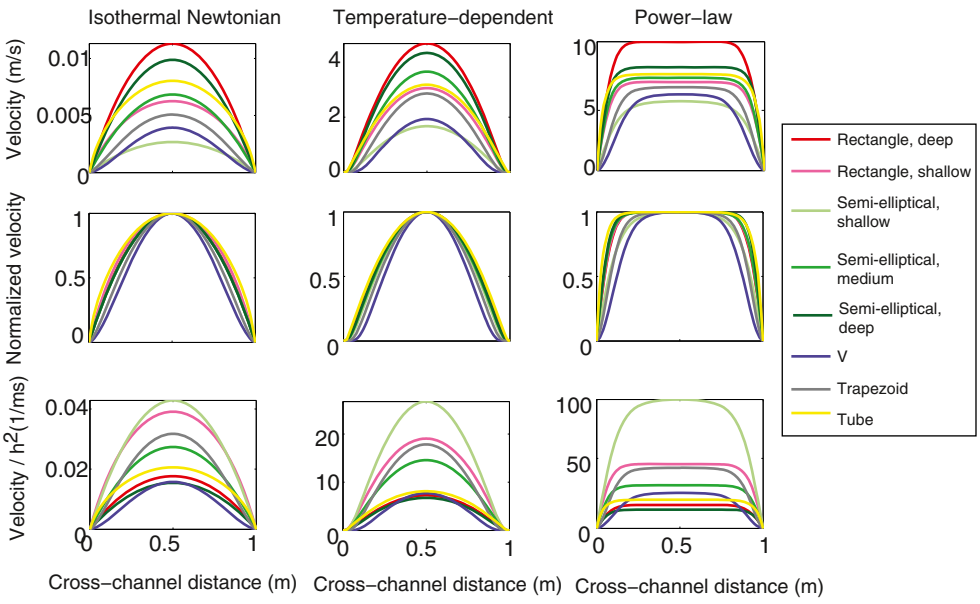

Fig. 4 Profiles across the velocity field at the surface of all our geometrical channels. *Top row* Velocity (m/s), *Middle row* Velocity normalized by maximum velocity for each flow, *Bottom row* Velocity normalized by the square of the each channel's depth. *Left column* Isothermal Newtonian; *Center column* Temperature-dependent models; *Right column* power law. Channels with similar shape and varying depth (e.g., all semi-elliptical ones) share a color, with varying darkness

rectangular channel geometry. The velocity profiles and table values indicate that surface velocity may be as low as just 65 % of the interior velocity (for a tube-like and a rectangle channel), in agreement with field observations (Pinkerton and Sparks 1976). For a shallow semi-elliptical channel geometry, the maximum velocity is found very close to the surface.

Discussion

After quantifying the inaccuracy introduced into viscosity and flux estimates by using an idealized geometric shape, the question arises as to which geometric approximation should be used when channel shape is not known. To answer this question, we evaluate the overall appropriateness of each approximation equation and channel shape by calculating the total misfit between inferred and input viscosities for the isoviscous models, where fit is defined by $\left(\sum_{models}\left(1-\frac{\eta_{inferred}}{\eta_{input}}\right)^2\right)^{\frac{1}{2}}$. For Newtonian fluids, total misfit values are 4.9, 1.86, and 1.42 for the Jeffreys equation, finite-width rectangle, and semi-elliptical channels, respectively. For models using a power-law fluid rheology, total misfit values were 22.99, 9.32, and 7.51, and for temperature-dependent Newtonian rheology: 12.3, 4.0, and 3.05. It appears, therefore, that when channel shape is not known, it is safest to use Eq. 4 and assume a semi-elliptical shape. For volumetric flux rates, the estimates obtained by using a finite-width approximation were overall closer (lower total misfit) than those obtained by the Jeffreys equation.

Channel shape versus alternative sources of inaccuracy

It is useful to compare the magnitude of flux and viscosity estimation errors resulting from assuming an inaccurate channel shape with errors stemming from uncertainties in flow depth. As discussed in length by Harris et al. (2007), field measurements of flow depths are difficult and assumptions are often made such that flow depth equals levee rim height. Similarly, velocities can naturally only be measured at the surface of the flow and might not represent the interior. It is also difficult to measure velocities if flow is within a tube with limited viewing points.

Examining Eq. 1a, one can see that an over/under estimation of flow depth by 10 % would lead to an over/underestimation of the viscosity by 20 %. If observers use Eq. 2 instead, an error in depth leads to an additional error in the "finite-width factor" β. The magnitude of this error depends on the aspect ratio of the channel, as can be seen from Fig. S2. The error in β is negligible for wide flows (Width/Depth$>$8) and comparable to the error in depth for narrow channels (Width/Depth$<$2).

As mentioned earlier, the overestimation of viscosity for an isothermal fluid with a Newtonian rheology due to employment of inappropriate analytical approximation can reach a factor of 3.5, and for the natural cases tested here the overestimation ranged from 16 to 40 %. Errors introduced by using an idealized channel shape equation such as Eqs. 1a, 2 or 4 are therefore comparable to or larger than those caused by inaccuracies in flow thickness.

Influence of temperature

Since lava viscosity depends strongly on temperature, viscosity is usually greater and velocity can be slower close to the surface relative the flow interior. This difference between surface and interior velocities has been observed in the field—for example, Pinkerton and Sparks (1976) estimated that during the 1975 Etna eruption, crusts moved 30 % slower than the interior. Our results for a rectangular channel agree well with this observation. Thus, using surface velocity measurements to estimate the viscosity of the entire flow can lead to an error. Our models highlight the fact that the difference between surface and interior velocity depends not only on the temperature difference, but also on the channel shape. The largest contrast was found for a narrow rectangular channel and the lowest for a wide semi-elliptical channel. We find that viscosities inferred from the surface velocities were as high as 8.2 (Eq. 1a on a narrow rectangular channel) and as low as 1.34 (Eq. 4) times the effective viscosity in the model. Once again, the semi-elliptical approximation (Eq. 4) provides the closest fit, even for a rectangular channel.

Our simulations illustrate the similarities between the influence of the channel geometry and the channel thermal structure on the observed surface velocity field. In essence, the cooler edges influence a flow in a similar manner to a narrower channel for an isoviscous material. This is evident in the example given in Fig. 5, where we plot the normalized cross-channel velocity profile for flow in a rectangular channel with a temperature-dependent viscosity, which is almost identical to the profile of isoviscous material in a channel with a trapezoid cross-section. Therefore, a stronger viscosity difference between the flow boundaries and core will produce velocity profiles similar to those from a shallow channel.

Effect on flux estimates

Our results indicate that uncertainty in the channel cross-sectional shape can have a large effect on the reliability of flux estimations. In the results table, we compare the measured flux in the channel, calculated by

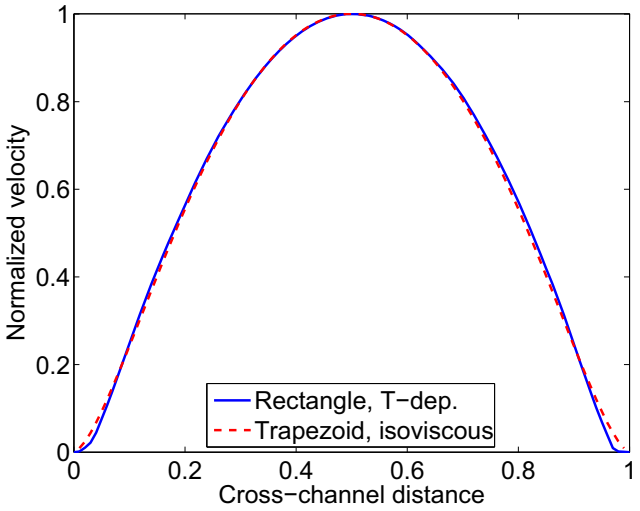

Fig. 5 Normalized velocity profiles across a *rectangular channel* with a temperature-dependent viscosity (*solid blue*) and a *trapezoid channel* with an isoviscous Newtonian viscosity (*dashed red*). The two profiles are almost identical, demonstrating the similar influence of temperature on a temperature-dependent flow to geometry on an isoviscous flow, on the observed surface velocity field

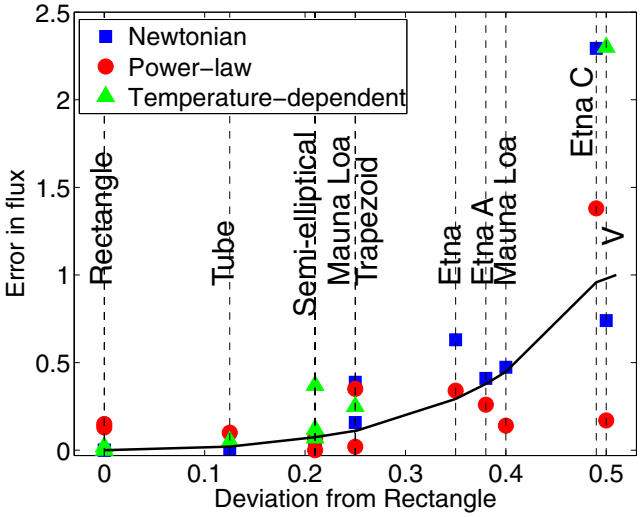

Fig. 6 Error in flux estimations for as a function of the channel's deviation from a rectangle. The error is defined as $|1 - \frac{flux\ calculated\ using\ Equation\ 3}{flux\ measured\ in\ models}|^2$. The horizontal axis gives the models' deviation from a rectangle, defined as $D = |1 - \frac{actual\ cross\ section\ area}{width \times depth}|$. Overall there is a positive proportionality between the error in flux and deviation from rectangle. However this relationship depends also on shape and rheology details. The *black curve* shows the error in flux caused solely by the cross-section area being smaller than the equivalent rectangle. This error is calculated as: $|1 - \frac{flux\ calculated\ using\ Equation\ 3\times(1-D)}{flux\ measured\ in\ models}|^2$. The difference between the markers and the *black curve* highlight the influence of the different distribution of velocities within each channel

numerically integrating the velocity over the model's cross-section area, with the flux predicted by entering the channel depth, width, and maximum velocity in Eqs. 1b and 3. For geometrically-shaped channels, both isothermal and temperature-dependent, Eq. 3 provides a better fit to the measured flux than Eq. 1b, while the opposite is true for the natural channels. For a power-law rheology, Eq. 3 gives a better fit also for the Hawaiian channels. It may be expected that the error in flux estimates will be proportional to the deviation of the shape from a rectangle, which we define as $D = 1 - \frac{actual\ cross\ section\ area}{width \times depth}$. Figure 6 shows the error in flux caused solely by the cross-section area being smaller than the equivalent rectangle (black curve). This error is calculated as: $\left|1 - \frac{flux\ calculated\ using\ Equation\ 3\times(1-D)}{flux\ measured\ in\ models}\right|^2$. The relationship between channel shape and flux estimation error is neither simple nor monotonic, and the shape of the channel influences the flux estimates differently for different rheologies and channels, due to the variable distribution of velocities within each flow.

Implications for interpreting old flows

The geometry of solidified lava flows is often used for the estimation of effusion rate and rheology in the absence of direct observations during flow emplacement. This is especially the case for submarine flows (Fundis et al. 2010) and for flows on other planets, where rheology can be used to infer chemical composition.

For flows on Ascraeus Mons, Mars, Hiesinger et al. (2007) calculated viscosities in the range of 5.52×10^4 to 2.86×10^7 Pa/s, depending on the analytical approximation used and the selected channel, but always assuming a rectangular channel. Based on cross-sections derived from MOLA data (Baloga et al. 2003), both V-shaped and a semi-elliptical channels are possible on Mars. If, in fact, the shape of the Ascraeus Mons channels is closer to a semi-circle, then the viscosities reported by Hiesinger et al. (2007) are approximately 15 % too high, and if closer to a V-shape, then the values would be two times too high. Our results suggest that the potential error would be smaller if a semi-elliptical channel approximation was used.

Conclusions

The influence of channel geometry on estimates of lava viscosity and mass flux made from measurements of surface velocity has been assessed using numerical models. Overall, errors introduced by assuming an inaccurate channel shape are comparable to, or even larger than those stemming from uncertainties in flow thickness, which is usually assumed to be the largest unknown. For Newtonian fluids, we find that channel shape alone can make the apparent viscosity of the flowing lava appear to be 3.5 greater (when applying the Jeffreys equation on a narrow semi-elliptical channel),

than it actually is. For a temperature-dependent rheology, a semi-elliptical analytical approximation yields apparent viscosity and flux values closer to input values than a rectangular analytical solution, for all channel shapes considered, including for rectangular channels. We also highlight a trade-off between channel shape and thermal structure, as both influence the internal velocities.

The analysis of viscosity estimation error for natural channels from Mauna Loa and Etna shows that if the lava is of Newtonian viscosity, a semi-elliptical analytical solution gives an approximation three times closer to the input viscosity than a rectangle with the same depth, while if the lava is shear-thinning (power law exponent $m = 0.6$), a rectangular approximation is 15 % more accurate. Volumetric flux for most natural channels we looked at is best approximated using an expression for an infinitely-wide sheet flow.

In conclusion, we recommend that our results be used to bracket possible viscosity and flux estimates when such values need to be assessed rapidly, for example during an eruption, and when channel-scale details of pre-eruption topography are unknown. In addition, the demonstrated importance of knowing the shape of lava channels implies further research should be done to characterize the statistical distribution of channel cross-section shapes and the representation of various end-member geometries in different environments.

Acknowledgments EL was supported during this work by the NSF grant EAR-1118943. Hannah Dietterich is thanked for processing the Mauna Loa lidar data. We thank the two reviewers of this paper, Jesse Robertson and Oryaelle Chevrel, and editor Matt Patrick, for their thorough and thoughtful reviews, which helped to improve this manuscript.

References

Bailey JE, Harris A, Dehn J, Calvari S, Rowland S (2006) The changing morphology of an open lava channel on Mt. Etna Bull Volcanol 68:497–515. doi:10.1007/s00445-005-0025-6

Baloga SM, Glaze LS, Crisp JA, Stockman SA (1998) New statistics for estimating the bulk rheology of active lava flows: Pu'u 'O'o examples. J Geophys Res 103(B3):5133–5142

Baloga SM, Mouginis-Mark PJ, Glaze LS (2003) Rheology of a long lava flow at Pavonis Mons. Mars J Geophys Res (Planets) 108(E7):5066. doi:10.1029/2002JE001981

Barrett R, Berry M, Chan T, Demmel J, Donato J, Dongarra J, Eijkhout V, Pozo R, Romine C, Van der Vorst H (1994) Templates for the solutions of linear systems: Building blocks for iterative methods. Society for Industrial and Applied Mathematics (SIAM), Philadelphia

Batchelor G (1967) An introduction to fluid mechanics. Cambridge University Press, Cambridge

Behncke B, Neri M, Nagay A (2005) Lava flow hazard at Mount Etna (Italy): new data from a GIS-based study. In: Manga M, Ventura G (eds) Kinematics and dynamics of lava flows. GSA Special Papers 395, pp 189-208. doi:10.1130/0-8137-2396-5.189

Chevrel MO, Platz T, Hauber E, Baratoux D, Lavallée Y, Dingwell DB (2013) Lava flow rheology: a comparison of morphological and petrological methods. Earth Planet Sci Lett 384:109–120

Crisci G, Iovine G, Di Gregorio S, Lupiano V (2008) Lava-flow hazard on the SE flank of Mt. Etna (Southern Italy). J Volcanol Geotherm Res 177:778–796

Crisp J, Cashman KV, Bonini JA, Hougen SB, Pieri DC (1994) Crystallization history of the 1984 Mauna Loa lava flow. J Geophys Res 99:7177–7198. doi:10.1029/93JB02973

Fink JH, Griffiths RW (1990) Radial spreading of viscous-gravity currents with solidifying crust. J Fluid Mech 221:485–509. doi:10.1017/S0022112090003640

Fink JH, Zimbelman JR (1986) Rheology of the 1983 Royal Gardens basalt flows, Kilauea Volcano, Hawaii. Bull Volcanol 48:87–96. doi:10.1007/BF01046544

Fulcher GS (1925) Analysis of recent measurements of the viscosity of glasses. J Amer Ceram Soc 8:339–355. doi:10.1111/j.1151-2916.1925.tb16731.x

Fundis AT, Soule SA, Fornari D, Perfit MR (2010) Paving the seafloor: Volcanic emplacement processes during the 2005–2006 eruptions at the fast spreading east pacific rise, 9'50. N Geochem Geophys Geosys 11(8):Q08024

Giordano D, Russell J, Dingwell D (2008) Viscosity of magmatic liquids: a model. Earth Planet Sci Lett 271:123–134

Gregg TKP, Fink JH (2000) A laboratory investigation into the effects of slope on lava flow morphology. J Volcanol Geotherm Res 96:145–159. doi:10.1016/S0377-0273(99)00148-1

Gregg TKP, Keszthelyi LP (2004) The emplacement of pahoehoe toes: Field observations and comparison to laboratory simulations. Bull Volcanol 66:381–391. doi:10.1007/s00445-003-0319-5

Griffiths RW, Kerr RC, Cashman KV (2003) Patterns of solidification in channel flows with surface cooling. J Fluid Mech 496:33–62. doi:10.1017/S0022112003006517

Harris AJL, Allen JS (2008) One-, two-, and three-phase viscosity treatments for basaltic lava flows. J Geophys Res 113(b12):B09212. doi:10.1029/2007JB005035

Harris AJL, Dehn J, Calvari S (2007) Lava effusion rate definition and measurement: a review. Bull Volcanol 70:1–22. doi:10.1007/s00445-007-0120-y

Harris AJL, Rowland SK (2001) FLOWGO: a kinematic thermorheological model for lava flowing in a channel. Bull Volcanol 63:20–44. doi:10.1007/s004450000120

Hauber E, Bleacher J, Gwinner K, Williams D, Greeley R (2009) The topography and morphology of low shields and associated landforms of plains volcanism in the Tharsis region of Mars. J Volc Geotherm Res 185(1):69–95

Hiesinger H, Head JW, Neukum G (2007) Young lava flows on the eastern flank of Ascraeus Mons: Rheological properties derived from high resolution stereo camera (HRSC) images and mars orbiter laser altimeter (MOLA) data. J Geophys Res (Planets) 112(e11):5011. doi:10.1029/2006JE002717

Hulme G (1974) The interpretation of lava flow morphology. Geophys J Int 39:361–383. doi:10.1111/j.1365-246X.1974.tb05460.x

Jaeger WL, Keszthelyi LP, Skinner JA, Milazzo MP, McEwen AS, Titus TN, Rosiek MR, Galuszka DM, Howington-Kraus E, Kirk RL, Team HiRISE (2010) Emplacement of the youngest flood lava on Mars: a short, turbulent story. Icarus 205:230–243. doi:10.1016/j.icarus.2009.09.011

James MR, Pinkerton H, Robson S (2007) Image-based measurement of flux variation in distal regions of active lava flows. Geochem Geophys Geosys 8:Q03006. doi:10.1029/2006GC001448

Jeffreys H (1925) Lxxxiv. the flow of water in an inclined channel of rectangular section. Lond Edinb Dublin Philos Mag J Sci 49(293):793–807

Johnson A (1970) Physical processes in geology. W.H. Freeman, New York

Johnson A, Rodine J (1984) Debris flow. In: Brunsden D, Prior D (eds) Slope instability. Wiley, New York, pp 257–361

Kauahikaua J (2007) Lava flow hazard assessment, as of August 2007, for Kīlauea East Rift Zone Eruptions, Hawai'i Island US Geol Surv. Open File Rep 1264(9)

Kilburn CRJ (2000) Lava flows and flow fields. In: Sigurdsson H., Houghton BF, McNutt SR, Rymer H, Stix J., McBirney AR (eds) Encyclopedia of volcanoes. Academic Press, San Diego, pp 291–305

Lipman PW, Banks NG (1987) AA flow dynamics, Mauna Loa 1984. In: Decker RW, Wright TL, Stauffer PH (eds) Volcanism in Hawaii. US Geol Surv Prof Pap, vol 1350, pp 1527–1567

Mazzarini F, Pareschi MT, Favalli M, Isola I, Tarquini S, Boschi E (2005) IMorphology of basaltic lava channels during the Mt. Etna September 2004 eruption from airborne laser altimeter data. Geophys Res Lett 32:L04305. doi:10.1029/2004GL021815

Moore HJ (1987) Preliminary estimates of the rheological properties of 1984 Mauna Loa lava. In: Decker RW, Wright TL, Stauffer PH (eds) Volcanism in Hawaii. US Geol Surv Prof Pap, vol 1350, pp 1569–1588

Nichols RL (1939) Viscosity of lava. J of Geol:290–302

Patrick MR, Dehn J, Dean K (2004) Numerical modeling of lava flow cooling applied to the 1997 Okmok eruption: Approach and analysis. J Geophys Res 109(b18):3202. doi:10.1029/2003JB002537

Pinkerton H (1978) Field measurements of the rheology of lava. Nature 276:383–385. doi:10.1038/276383a0

Pinkerton H, Sparks RSJ (1976) The 1975 sub-terminal lavas, mount etna: a case history of the formation of a compound lava field. J Volcanol Geotherm Res 1(2):167–182

Pinkerton H, Wilson L (1994) Factors controlling the lengths of channel-fed lava flows. Bull Volcanol 56:108–120. doi:10.1007/BF00304106

Robertson J, Kerr R (2012a) Isothermal dynamics of channeled viscoplastic lava flows and new methods for estimating lava rheology. J Geophys Res 117(B1):B01202

Robertson J, Kerr R (2012b) Solidification dynamics in channeled viscoplastic lava flows. J Geophys Res 117(B7):B07206. doi:10.1029/2012JB00916

Sakimoto SEH, Gregg TKP (2001) Channeled flow: Analytic solutions, laboratory experiments, and applications to lava flows. J Geophys Res 106:8629–8644. doi:10.1029/2000JB900384

Shaw HR (1969) Rheology of basalt in the melting range. J Petrol 10:510–535

Sonder I, Zimanowski B, Büttner R (2006) Non-Newtonian viscosity of basaltic magma. Geophys Res Lett 33:L02303. doi:10.1029/2005GL024240

Spera FJ, Borgia A, Strimple J, Feigenson M (1988) Rheology melts and magmatic suspensions. I - design and calibration of concentric cylinder viscometer with application to rhyolitic magma. J Geophys Res 93:10273–10294. doi:10.1029/JB093iB09p10273

Takagi D, Huppert HE (2007) The effect of confining boundaries on viscous gravity currents. J Fluid Mech 577(1):495–505

Tallarico A, Dragoni M (1999) Viscous Newtonian laminar flow in a rectangular channel: Application to Etna lava flows. Bull Volcanol 61:40–47. doi:10.1007/s004450050261

Walker GPL (1968) Thickness and viscosity of Etnean lavas. Nature 213:484–485. doi:10.1038/213484a0

Walker GPL (1973) Lengths of lava flows. Phil Trans R Soc Lond 274:107–118

Zimbelman JR (1998) Emplacement of long lava flows on planetary surfaces. J Geophys Res 103:27503–27516. doi:10.1029/98JB01123